Detectability prospects for long-lived γ-ray emission from r-process events

Benjamin Amend ,[1,2] Christopher L. Fryer ,[1] Matthew R. Mumpower ,[3,4] and Oleg Korobkin [4]

[1] *Center for Nonlinear Studies, Los Alamos National Laboratory, Los Alamos, NM 87545 USA*
[2] *Department of Physics and Astronomy, Clemson University, Clemson, SC 29634, USA*
[3] *Theoretical Division, Los Alamos National Laboratory, Los Alamos, NM 87545 USA*
[4] *Center for Theoretical Astrophysics, Los Alamos National Laboratory, Los Alamos, NM 87545 USA*

ABSTRACT

Detecting gamma-ray emission from radioactive decay in r-process-enriched kilonova and supernova remnants offers a direct method for probing heavy element synthesis in the Milky Way. We assess the feasibility of such detections through an all-sky survey using mock instruments similar to the COmpton Spectrometer and Imager (COSI) and targeted observations with sensitive, low field-of-view instruments similar to the High Energy X-ray Probe (HEX-P). By modeling the spatial distribution of potential remnants and generating synthetic time-evolving gamma-ray spectra, we compare predicted fluxes to the sensitivity limits of each instrument. Our findings suggest that the likelihood of detecting kilonova remnants with COSI-like instruments over a 24-month observing cycle is extremely low ($\sim$1%), highlighting the need for instruments with at least ten times greater sensitivity to make such detections more probable. The superior sensitivity of a HEX-P-like instrument offers higher chances of detection, provided suitable targets are identified. We propose methods for optimizing target selection and outline the observational advancements needed to improve detectability prospects. Both detections and non-detections carry important implications for our understanding of galactic r-process nucleosynthesis, influencing future observational strategies.

1. INTRODUCTION

Approximately half of all chemical elements heavier than iron are produced via the rapid neutron capture process, or r-process (Burbidge et al. 1957; Cameron 1957; Seeger et al. 1965). Proposed astrophysical sites for the r-process can broadly be classified as massive stellar collapses (perhaps magnetorotationally- or fallback-driven) (Siegel et al. 2019; Nishimura et al. 2015; Winteler et al. 2012; Yong et al. 2021; Woosley et al. 1994; Wanajo et al. 2001; Fryer et al. 2006) and compact binary mergers (CBMs) involving at least one neutron star (Eichler et al. 1989; Freiburghaus et al. 1999; Lattimer & Schramm 1974; Korobkin et al. 2012; Just et al. 2015; Bauswein et al. 2013; Wanajo et al. 2014; Rosswog et al. 1999; Hotokezaka et al. 2013; Goriely et al. 2011; Surman et al. 2008), although rarer more exotic events have also been proposed (for an excellent review on this subject, refer to Cowan et al. (2021)). The relative contributions to the r-process between these source classes is still regarded as an open

question, one that many galactic chemical evolution models have sought to address (e.g. Argast et al. (2004); Matteucci et al. (2014); Côté et al. (2019)). These models rely heavily on accurate r-process yields; because there is limited experimental data on many of the heavy, neutron-rich isotopes that are relevant to the r-process, these yields have traditionally been estimated from nuclear models (e.g, Korobkin et al. 2012). Since 2017, these estimates have been supplemented by additional astrophysical constraints from the neutron star-neutron star merger GW170817 (Pian et al. 2017; Tanvir et al. 2017). But due to uncertainties in modeling the light curve of the associated kilonova AT2017gfo (Zhu et al. 2021; Barnes et al. 2021), the yields are still ambiguous, and much of the relevant nuclear physics remains unknown (Schatz et al. 2022). Additional observations of r-process events are therefore necessary to more robustly constrain these features.

Detecting r-process signatures in relevant astrophysical events - e.g. supernovae and kilonovae - has posed significant observational challenges. Kilonovae are ex-

ceedingly rare events and, while several potential candidates have been identified (Rastinejad et al. 2022; Tanvir et al. 2013; Berger et al. 2013; Jin et al. 2015; Kasliwal et al. 2017), it is difficult to prove these transients are neutron star mergers, let along determine their r-process signature. The concurrent gravitational wave detection (GW170817) of AT2017gfo demonstrated that this even is indeed a neutron star merger, but uncertainties in the initial analysis of this transient predicted a wide range of r-process yields (Côté et al. 2019). Subsequent studies modeling kilonova have demonstrated the degeneracies in modeling the light-curves including everything from morphology (Korobkin et al. 2021) to velocity distribution (Tak et al. 2023; Fryer et al. 2024). Spectral features have also proved problematic where line features can be explained by different interpretations (Watson et al. 2019; Tarumi et al. 2023) and disentangling atomic line identifications has proven problematic. Since the r-process yields from stellar collapse tend to be buried within the ejecta, observation spectral signatures of these elements in supernovae or collapsars is even more difficult.

Detection prospects for both types of sources may improve upon shifting the observational frequency range from optical/infrared to hard X-rays/gamma rays. At these wavelengths, radioactive decay, not atomic line features, drives the emission (Hotokezaka et al. 2016; Li 2019). Some of the decay processes that produce these photons are relatively long-lived ($\gtrsim 100\,$kyr) and as such, older kilonova or supernova remnants within the Milky Way may be viable observational targets. After the first year, this high-energy emission does not depend on transport effects and only mildly affected by the ejecta properties. In addition, the line features can not be confused with the emission from lighter elements. As such, these decay photons provide a more direct window into the yields.

Over the last few years, a few studies have been published on the detectability prospects of long-lived gamma ray emission from local kilonova remnants. Wu et al. (2019) use observed short gamma ray burst (sGRB) offsets to model the locations of these remnants in the sky, assigning them individual line fluxes and comparing to threshold sensitivity values of proposed next-generation MeV γ-ray instruments. The observed sGRB offset distribution includes projected offsets from bursts in a variety of different host galaxies (Fong et al. 2022), and while this could potentially reflect the kilonova remnant distribution within our own galaxy (Gaspari et al. 2023), this is not guaranteed given the differences in host mass, morphology, and age (though the authors attempt a first pass at accounting for this by consider-

ing two distinct models that use either host-normalized offsets or pure physical offsets). Korobkin et al. (2020) place greater emphasis on the nuclear physics, synthesizing full spectra in the $\sim 10\,$keV$-$MeV range rather than focusing on just a few prominent lines. However, they only consider remnants at exact distances of 3 kpc and 10 kpc, contrasting with the broad spectrum of distances that arise naturally from the remnant distributions generated in Wu et al. (2019). Terada et al. (2022) also performed detailed nuclear network simulations of r-process nucleosynthesis in neutron star merger remnants, focusing on the gamma-ray emissions over long timescales and proposing diagnostics based on gamma-ray line ratios for electron fraction and remnant age. Distance limits for detectable events were discussed, but the possible distribution of neutron star merger sites was not explored beyond the assumption of the isotropic population also assumed in Wu et al. (2019). Supernovae were also not considered, and the work was generally intentionally agnostic to a specific instrument, outside of the brief discussion towards the end (which included many current and future gamma-ray and hard X-ray missions, but not COSI or HEXP-like instruments).

In this work, we aim to build upon these prior studies in the specific context of a wide-field gamma-ray instrument analogous to COSI, and a highy sensitive narrow-field X-ray instrument akin to HEX-P. We model various distributions of galactic kilonova and supernova remnants, produce time-evolving synthetic gamma ray spectra for the decay of several r-process isotopes at late stages in remnant evolution, and compare predicted hard X-ray and gamma ray fluxes to the relevant instrument sensitivities.

This paper is organized as follows. In Sec. 2, we present models for the distribution of galactic kilonova remnants from compact binary mergers that have occurred within the past 1 Myr; these models include orbit integrators in the context of static and time-evolving galactic potentials. We present a similar model distribution of recent galactic supernova remnants in Sec. 3. We then discuss the properties of both the kilonova and supernova remnants in Sec. 4, and present synthetic spectra for the radioactive decay associated with long-lived r-process isotopes in Sec. 5. We discuss the detection capabilities of COSI and HEX-P-like instruments in Sec. 6, and present detectability prospects for r-process events for each instrument. Finally, we conclude with a summary of our results and a brief discussion on the implications of our predictions in Sec. 7.

2. KILONOVA REMNANT DISTRIBUTION

While galactic supernova remnants are largely confined to the disk spiral arms, the distribution of galactic kilonova remnants is likely more extended due to the unique nature of their compact binary progenitor systems. Simple comparison of the galactocentric offset distributions for long and short gamma ray bursts (associated with supernovae and kilonovae, respectively) appears to yield evidence for this (Blanchard et al. 2016; Fong et al. 2022). However, these bursts are observed in a variety of different galaxies, all with distinct morphologies and formation histories. Furthermore, because only projected offsets can be measured, we have a limited picture of the burst locations in 3D space relative to their galactic centers. As such, the true spatial distribution of these bursts is somewhat poorly constrained. To combat these uncertainties, we attempt to account for all possible scenarios by constructing four distinct models for the compact binary merger site distribution: isotropic model, disk model, static orbit model and dynamic orbit model.

Among these four models are two simple cases: in the isotropic model, we assume a perfectly isotropic distribution of compact binary merger sites using observed short gamma ray burst offsets to model the radial component of the distribution, and in the disk model we assume all mergers take place within the stellar disk of the Milky Way. These two models account for extreme cases that most likely bookend the true galactic kilonova remnant distribution. Additionally, we construct a static orbital model in which we integrate the orbits of compact binary systems in a static representation of the present-day galactic potential. This produces a physically-motivated distribution that is more extended than the disk, though it loses robustness if merger times are $\gtrsim 1\,\mathrm{Gyr}$ since it does not account for galactic evolution. We then formulate a dynamic orbital model in which we modify the static orbital model by time-evolving the galactic potential. This model retains the physical underpinnings of the static orbital model while better accommodating systems with merger times $\gtrsim 1\,\mathrm{Gyr}$, but it does so at the cost of certainty in the galactic potential parameters since the detailed formation history of the Milky Way is not well understood.

2.1. The Isotropic Model

If the velocities of compact binaries (driven by mass loss and supernova kicks) are strong relative to the escape speed of the galaxy, or if merger times are $\gtrsim$ the orbital periods of these systems about the galactic center, the kilonova remnant distribution should exhibit some level of isotropy. To model this, we utilize the method implemented in Wu et al. (2019), where the ob-

served short gamma-ray burst (sGRB) offset distribution is used to represent the radial distribution of galactic compact binary merger sites. We take advantage of the more recently published expanded catalog of sGRB offsets from Fong et al. (2022). Many of the burst host galaxies in this catalog are elliptical or irregular, and likely increase the mean of our isotropic distribution beyond what may be accurate for a Milky Way-like galaxy, but because this model is acting as a limiting case, this should not negatively impact its applicability. Radial positions are sampled from this offset distribution, and random angles are generated via

$$\theta = 2\pi u, \quad \phi = cos^{-1}(2v - 1) \quad u, v \in [0, 1), \quad (1)$$

where u, v are uniform random variables. Because these sGRB radial offsets have been observed in a variety of different types of host galaxies, with different sizes and morphologies, we opt to *only* test the host-normalized offsets, using an effective Milky Way radius of $5.75\,\mathrm{kpc}$ (Lian et al. 2024).

2.2. The Disk Model

If the binary velocities from mass loss and supernova kicks are weak relative to the galactic escape velocity, or merger times are short relative to galactocentric orbital periods, most compact binary systems will merge within the galactic disk. To represent this distribution, we model the stellar disk of the Milky Way with the thickened disk density profile presented in Miyamoto & Nagai (1975)

$$\rho_*(R, z) = \left(\frac{b_*^2 M_*}{4\pi}\right) \frac{a_* R^2 + \left(3\sqrt{z^2 + b_*^2} + a_*\right)\left(\sqrt{z^2 + b_*^2} + a\right)^2}{\left[R^2 + \left(\sqrt{z^2 + b_*^2} + a\right)^2\right]^{5/2} (z^2 + b_*^2)^{3/2}}.$$
$$(2)$$

The parameters M_*, a_*, and b_* have fixed values under the constraints that the present-day total stellar mass $M_{*,0}$, local surface stellar density $\Sigma_{*,0}$, and local volume stellar density $\rho_{*,0}$ are all accurately reproduced. We take $M_{*,0} = M_* = 6.08 \times 10^{11}\,\mathrm{M_\odot}$ from Licquia & Newman (2015), and the local stellar densities $\Sigma_{*,0} = 33.4\,\mathrm{M_\odot pc^{-2}}$ and $\rho_{*,0} = 0.043\,\mathrm{M_\odot pc^{-3}}$ from McKee et al. (2015), resulting in $a_* = 1.930\,\mathrm{kpc}$ and $b_* = 0.380\,\mathrm{kpc}$. We then obtain merger sites for this model via inverse transform sampling from this density function.

2.3. The Static Orbital Model

In reality, the merger times for compact binary systems are not universally long or short, but constitute a delay time distribution (DTD), and binary velocities

depend on the properties of the stars in their progenitor systems. As such, a model that integrates population synthesis data with orbital calculations embedded in a galactic potential may result in a more accurate compact binary merger distribution than a simplistic disk or isotropic model, although these can still be informative as limiting cases given uncertainties in more complicated models.

For this model, we construct a very simple galactic potential consisting of a stellar disk, a gaseous disk, and a dark matter halo. For both disks, in concordance with our disk density profiles, we use the potential from Miyamoto & Nagai (1975),

$$\Phi_{\mathrm{disk}}(R, z) = -\frac{GM}{\sqrt{R^2 + \left(\sqrt{z^2 + b^2} + a\right)^2}}\,, \quad (3)$$

where the parameters for the stellar disk are equivalent to those from Sec. 2.2. For the gaseous disk, parameter fitting necessitated a higher present-day gas mass value $M_{\mathrm{gas},0} = 1.465 \times 10^{10}\,\mathrm{M_\odot}$ than what is generally consistent with contemporary estimates (e.g. Flynn et al. (2006)). However, this mass in conjunction with $a_{\mathrm{gas}} = 5.673\,\mathrm{kpc}$ and $b_{\mathrm{gas}} = 0.167\,\mathrm{kpc}$ successfully reproduces the present-day local gas mass surface and midplane volume densities $\Sigma_{\mathrm{gas},0} = 13.7\,\mathrm{M_\odot pc^{-2}}$ and $\rho_{\mathrm{gas},0} = 0.041\,\mathrm{M_\odot pc^{-3}}$ from McKee et al. (2015).

We model the dark matter halo with the NFW profile (Navarro et al. 1996)

$$\Phi_{\mathrm{DM}}(r) = -\frac{4\pi G \rho_0 r_s^3}{r}\ln\left(1 + \frac{r}{r_s}\right), \quad (4)$$

where r_s is the scale radius and ρ_0 is the characteristic density. Adopting a cutoff radius $r_{\mathrm{max}} = 200\,\mathrm{kpc}$,

$$\rho_0 = \frac{M_{\mathrm{DM},0}}{4\pi r_s^3}\left[\ln\left(\frac{r_s + r_{\mathrm{max}}}{r_s}\right) - \frac{r_{\mathrm{max}}}{r_s + r_{\mathrm{max}}}\right]^{-1}. \quad (5)$$

We estimate the present-day mass of the Milky Way dark matter halo by subtracting our model stellar and gas masses from the total galactic mass $M_{\mathrm{vir}} = 1.54 \times 10^{12}\,\mathrm{M_\odot}$ (Watkins et al. 2019), resulting in $M_{\mathrm{DM},0} = 7.855 \times 10^{11}\,\mathrm{M_\odot}$. We then use a scale radius $r_s = 7.962\,\mathrm{kpc}$ such that the local dark matter mass density of $\rho_{\mathrm{DM},0} = 0.013\,\mathrm{M_\odot pc^{-3}}$ (McKee et al. 2015) is reproduced.

These three components - the stellar disk, the gaseous disk, and the dark matter halo - constitute the total galactic potential in which we integrate the orbits of compact binary systems (Fig. 1). To calculate these orbital trajectories, we first sample birthplaces from the stellar disk density function (Eq. 2), initializing their
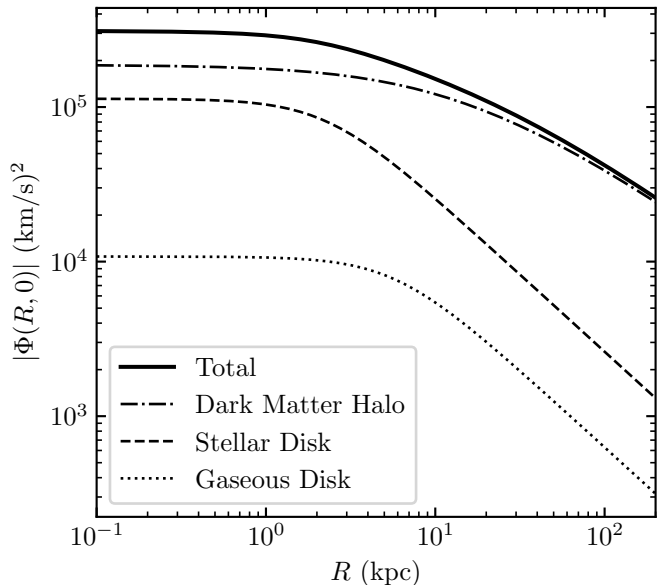

Figure 1. The absolute value of the midplane galactic potential from our static orbital model. The dark matter halo, being the most massive component, largely dominates the potential, with secondary contributions from the stellar and gaseous disks at smaller radii.

motion with circular velocities about the galactic center,

$$v_c(R) = \sqrt{R\frac{d\Phi(R, z=0)}{dR}}\,. \quad (6)$$

We then draw delay times and binary velocities from the population synthesis models M.380B and M.480B presented in Olejak et al. (2021) - variants of the `StarTrack` population synthesis code initially developed to model evolutionary pathways of stellar populations, including compact object binaries (Belczynski et al. 2002, 2008). The delay time and systemic kick velocity distributions from the `StarTrack` data are shown in Figs. 2 & 3. Systems evolve for the duration of these delay times and their systemic velocities are modified by supernova kicks up until the inspiral times (Fig. 4), when the spatial coordinates of the merger are recorded. Most events remain bound to the galaxy, but a small fraction ($\sim 1 - 2\%$) are ejected and merge outside the Milky Way's virial radius.

2.4. *The Dynamic Orbital Model*

Population synthesis models, including those used in the previous section, indicate that merger timescales for compact binary systems can be as long as $\sim 1 - 10\,\mathrm{Gyr}$ (Blanchard et al. 2017; Voss & Tauris 2003; Belczynski et al. 2006; Fryer et al. 1999; Bloom et al. 1999). The subset of NS-NS / BH-NS systems that have merged within the last $\sim 1\,\mathrm{Myr}$ likely includes several of these long-delay systems, and as such the time dependence
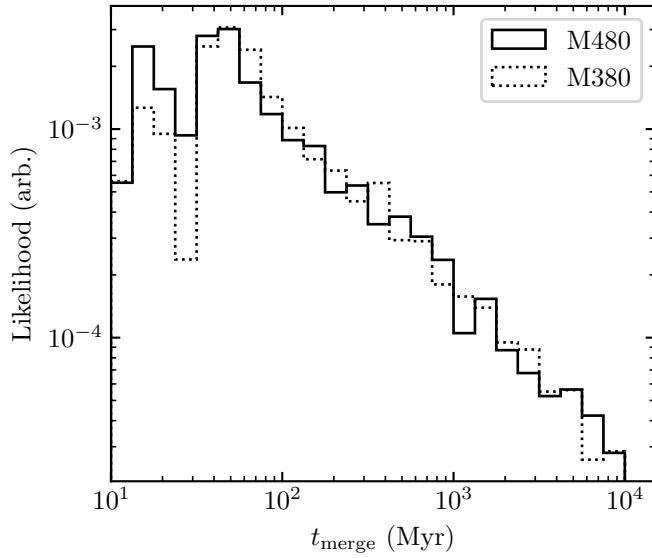
Figure 2. The neutron star-neutron star merger delay time distribution from `StarTrack` models M380 and M480 for solar metallicity. The two models are very similar to each other, and both scale as $\sim t_{\mathrm{merge}}^{-1}$ for all but the fastest mergers.
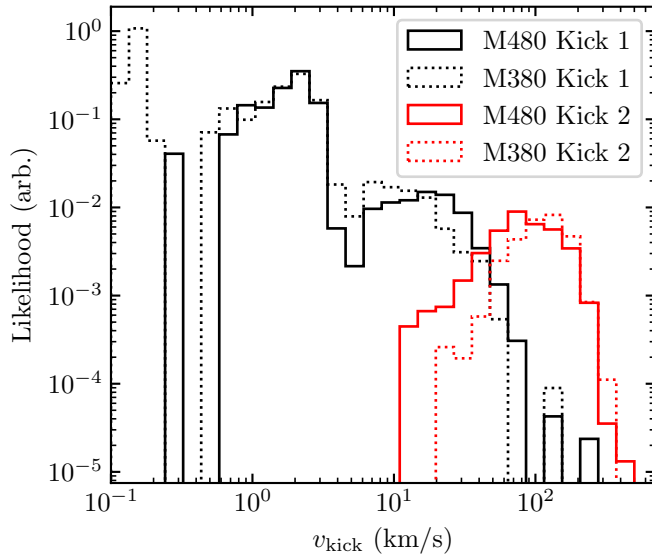

Figure 3. The neutron star-neutron star merger kick velocity distributions from `StarTrack` models M380 and M480 for solar metallicity. The distribution of velocities for the first supernova kick (black) is quite broad in comparison to the second supernova kick (red), which tends to favor higher velocities $\sim 100 \, \mathrm{km/s}$.

of the galactic environment may be important in accurately determining merger locations (Wiggins et al. 2018).

Galaxy formation and evolution are incredibly complex processes that encompass many different subfields of physics and astrophysics, and attempting to model

these processes accurately for any one particular galaxy is nontrivial. While some trends can be inferred from present-day properties of the Milky Way itself (Helmi et al. 1999; Belokurov et al. 2018; Helmi et al. 2018; Myeong et al. 2019), snapshots of other morphologically similar galaxies at different redshifts (see Conselice (2014) for a detailed review), and simulations ranging in scale from sub-galactic to cosmological (Frankel et al. 2019), the detailed history of our own Milky Way galaxy is still not fully understood. There is substantial evidence that the Milky Way has undergone at least 6 distinct merger events throughout its life (Malhan et al. 2022), and this is to say nothing about additional (non-merger) gravitational interactions with other massive systems. Since the galactic potential acts here as a backdrop for our study rather than the subject of the study itself, we construct what should be seen as a toy model which captures the essence of the growth of a galaxy, modeling time-dependent masses and scale lengths for simple analytic potential profiles. To do this, we modify the three components from our static orbital model, utilizing time-dependent prescriptions from various works throughout the literature on galactic properties and evolution - an approach analogous to the one outlined in Zevin et al. (2020).

We begin by taking the stellar mass M_* to be the result of integrating the star formation rate $\psi(t)$, which we assume to have a delayed-tau form as motivated by Speagle et al. (2014) and Madau & Dickinson (2014), where

$$\psi(t) = At e^{-t/\tau}. \tag{7}$$

Integrating this from $t' = 0$ to $t' = t$ then yields an analytic expression for the stellar mass $M_*(t)$ as a function of time t,

$$M_*(t) = A \left[\tau^2 - e^{-t/\tau} \left(\tau^2 + t\tau \right) \right]. \tag{8}$$

Precise values for A and τ can be determined given the present-day observed values of M_* and ψ in the Milky Way. Fixing the present-day stellar mass at $6.08 \times 10^{11} \, \mathrm{M_\odot}$ as we did in Sec. 2.2 while also setting $\psi_0 = 1.65 \, \mathrm{M_\odot yr^{-1}}$ (Licquia & Newman 2015), we determine $A = 5.238 \times 10^9 \, \mathrm{M_\odot \cdot Gyr^{-2}}$ and $\tau = 3.612 \, \mathrm{Gyr}$.

The scaling behavior of the time evolution of the radial scale length a_* for the stellar disk is modeled after the best-fit results from Nelson et al. (2016), but we renormalize the expression so that the present-day local stellar surface density as reported in McKee et al. (2015) is reproduced. Assuming a solar orbital radius of $8.1 \, \mathrm{kpc}$,

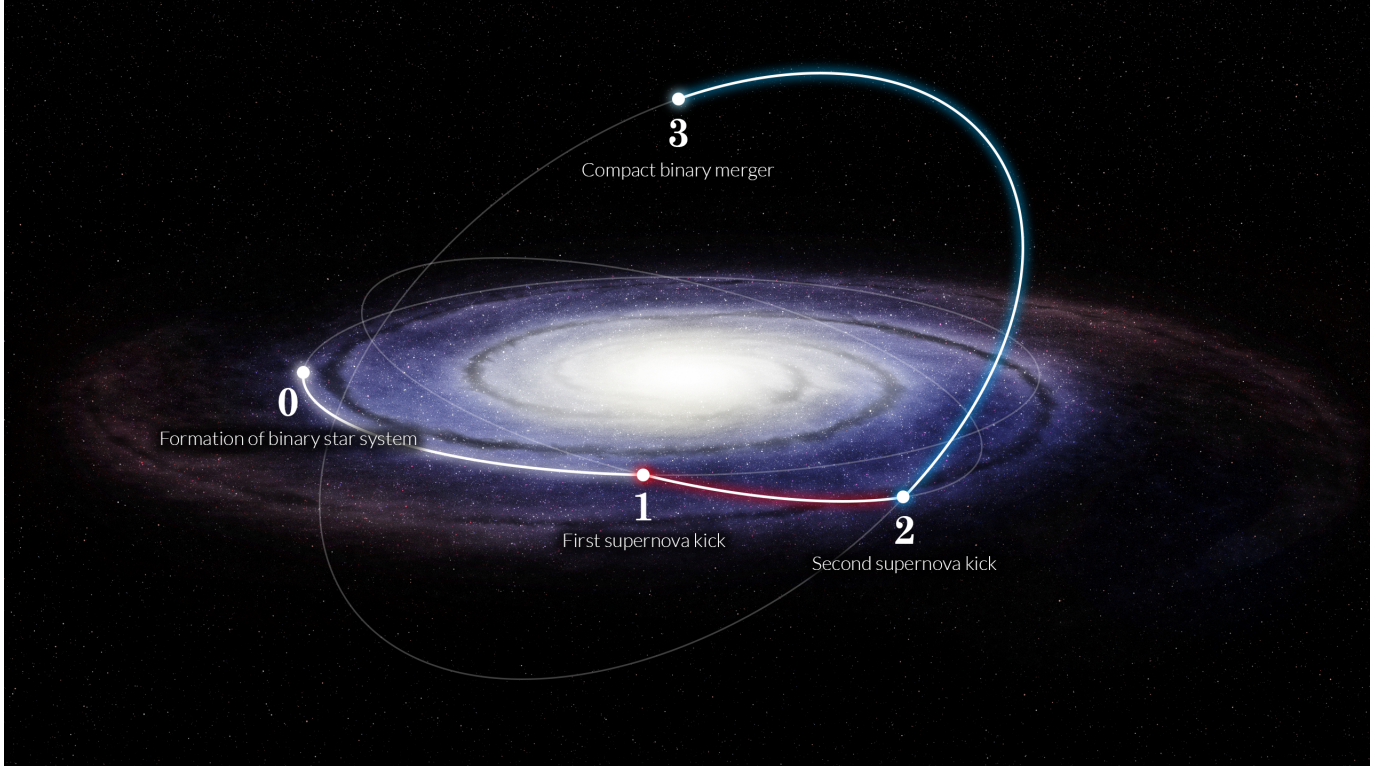$$a_*(t) = 1.405 \left[\frac{M_*(t)}{10^{10} \, \mathrm{M_\odot}} \right]^{0.176} \mathrm{kpc}. \tag{9}$$

Figure 4. A representative illustration of an orbital trajectory for a compact binary merger, from the birth of its progenitor stars to its ultimate inspiral. Point **0** represents the coordinates where a main sequence 'binary' is initialized with a circular velocity in the galactic disk. At point **1** one of the stars in the binary undergoes a supernova and imparts a kick, modifying the systemic orbital velocity and inclining the orbital plane. The other star later undergoes a supernova at point **2**, imparting a second kick and again changing the systemic orbital velocity and orbital plane inclination. The compact remnants from these two supernovae ultimately merge at point **3**.

We determine the mass $M_\mathrm{g}(t)$ of the gaseous disk by assuming a Kennicutt-Schmidt star formation law (Schmidt 1959; Kennicutt 1989, 1998) and inverting the star formation rate as outlined in Lilly et al. (2013),

$$M_\mathrm{g}(t) = \left[\frac{\psi(t)}{\alpha}\right]^{1/1.4}, \qquad (10)$$

where α is the star formation rate efficiency. We set $\alpha = 9.668 \times 10^{-6}$ such that the best-fit present-day observed Milky Way gas mass as reported in Flynn et al. (2006) is reproduced.

We assume that the radial scale length of the gaseous disk is proportional to radial scale length of the stellar disk throughout the evolution of the galaxy, so we further rescale the relation in Eq. 9 in an attempt to reproduce the present-day local gaseous surface density reported in McKee et al. (2015),

$$a_\mathrm{g}(t) = 2.939 a_*(t). \qquad (11)$$

We assume similar scaling relations for the vertical scale heights, and choose the normalization factors such that the present-day local stellar and gaseous volume mass densities as reported in McKee et al. (2015) are accurately reproduced. Then

$$b_*(t) = 0.197 a_*(t) \qquad (12)$$

and

$$b_\mathrm{g}(t) = 0.0294 a_\mathrm{g}(t) \qquad (13)$$

We model the mass M_DM of the dark matter halo as a simple exponential in redshift,

$$M_\mathrm{DM}(z) = M_\mathrm{DM,0} e^{-pz}, \qquad (14)$$

and find $p = 0.367$ under the assumption that $M_\mathrm{DM,0} = 7.855 \times 10^{11}\,\mathrm{M_\odot}$ (Sec. 2.3). The scale radius r_s relates to the virial radius r_vir and the concentration c via

$$r_s = \frac{r_\mathrm{vir}}{c}, \qquad (15)$$

where we take

$$r_\mathrm{vir} = \left(\frac{3M_\mathrm{DM}}{4\pi\Delta\rho_c}\right)^{1/3} \qquad (16)$$

and $\Delta = 200$. The critical density ρ_c is

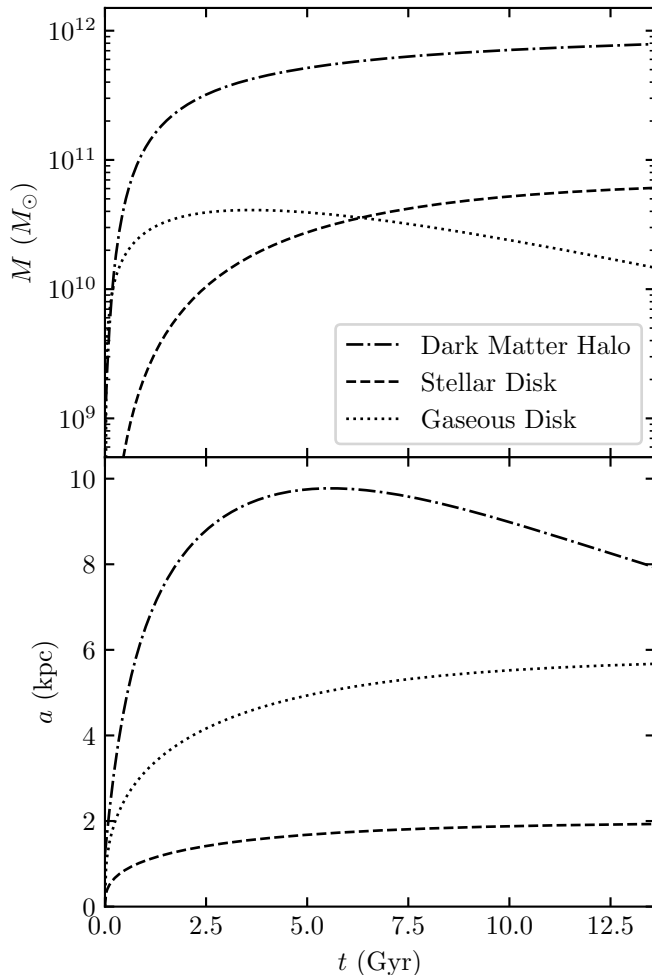$$\rho_c = \frac{3H^2}{8\pi G}, \qquad (17)$$

Figure 5. Time evolution of the masses (top) and radial scale lengths (bottom) of the dark matter halo, stellar disk, and gaseous disk. The contraction following the expansion of the dark matter halo is an expected result consistent with predictions outlined in Klypin et al. (2011).

where

$$H = H_0 \sqrt{\Omega_m (1+z)^3 + \Omega_\Lambda}. \qquad (18)$$

We adopt the most recent Planck cosmological parameters for this work, where $\Omega_m = 0.315$ and $H_0 = 67.4 \, \mathrm{km \cdot s^{-1} \cdot Mpc^{-1}}$ (Planck Collaboration et al. 2020), with $\Omega_\Lambda = 1 - \Omega_m = 0.685$.

We assume the concentration parameter c scales with redshift as

$$c = \frac{c_0}{1+z}, \qquad (19)$$

where $c_0 = 24.384$ by fixing $r_{s,0} = 7.962 \, \mathrm{kpc}$ (Sec. 2.3).

Fig. 5 shows the time evolution of the masses and radial scale lengths of each of the three components in our model.

We integrate orbits in a similar fashion to Sec. 2.3 - however, the birth times of merging compact binary systems have a substantial impact on their orbital evolution and merger locations due to the time-dependence of the galactic potential, and as such it is crucial to accurately represent the distribution of these birth times for mergers that have occurred within the last $10^6 \, \mathrm{yr}$ (our window of interest). The distribution χ of birth times t' for systems that merge between time t (13.599 Gyr) and $t + \Delta t$ (13.6 Gyr) can be obtained by convolving the delay time distribution with the star formation rate, and integrating over coordinate time from t to $t + \Delta t$:

$$\chi(t, t') \propto \int_t^{t + \Delta t} f(t') \mathrm{DTD}(\tilde{t} - t') \psi(t') \, d\tilde{t}. \qquad (20)$$

The function $f(t')$ represents the fraction of stars born at time t' that will ultimately merge as compact objects. Assuming this fraction is constant in time, and that $\mathrm{DTD}(t) \propto t^{-1}$ with a minimum delay time of 20 Myr, this integral can be solved analytically with our delayed-tau star formation rate. Thus,

$$\chi(t, t') \propto t' e^{-t'/\tau} \ln \left| \frac{t + \Delta t - t'}{t - t'} \right|, \qquad (21)$$

where $(t - t') \geq 20 \, \mathrm{Myr}$. This distribution features a broad peak for long mergers corresponding to the epoch of peak star formation, and a secondary sharp spike at current time t characterized by fast mergers, and we sample from $\chi(t, t')$ to obtain the birth times of compact binary systems in any given model instance.

The population synthesis data also exhibits weak metallicity dependencies. To estimate the metallicities of the compact binary systems, we sample from a simple normal distribution with a mean given by the redshift-dependent prescription outlined in Madau & Fragos (2017),

$$\log \langle Z/Z_\odot \rangle = 0.153 - 0.074 z^{1.34}, \qquad (22)$$

and standard deviation $\sigma = 0.2 \, \mathrm{dex}$ motivated by analysis of scatter in the age-metallicity relation (Nordström et al. 2004; Holmberg et al. 2007; Feltzing et al. 2001). The resultant redshift-metallicity relation is shown in Fig. 6.

2.5. *Compact Binary Merger Site Distributions*

The physical offset distributions for each of our models are shown in Fig. 7. The mean of the static orbital model offset distribution is only $\sim 25\%$ greater than the mean of the disk offset distribution - this modest increase is consistent with estimates for offsets in large spiral galaxies, e.g. Belczynski et al. (2006). The dynamic orbital model produces even smaller offsets due to the smaller disk scale lengths at early times. The isotropic distribution has a much larger mean, possibly due to observational biases, stronger kick velocities/longer merger
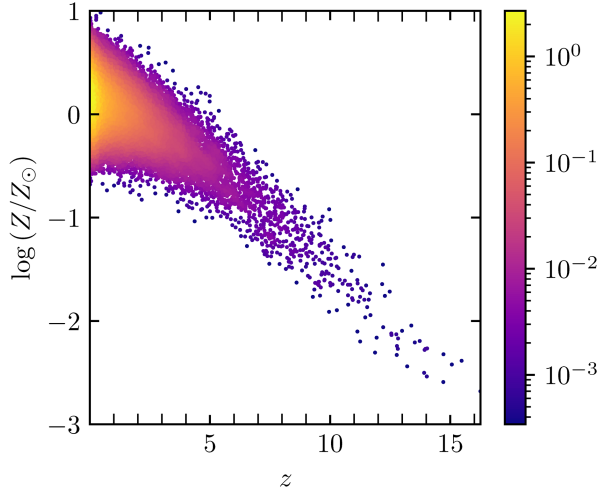
Figure 6. A representative sampling of the redshift-metallicity relation used in our dynamic orbital model. Samples are drawn from a Gaussian distribution with a mean given by Eq. 6 in Madau & Fragos (2017) and a standard deviation of 0.2.

times, and/or variation in host galaxy morphology. Additionally, the dynamic model only includes systems that would have merged within the last 1 Myr, and this selective bias may change the statistics.

3. SUPERNOVA REMNANT DISTRIBUTION

While kilonovae are exceedingly rare events, supernovae are much more common, and as such there are hundreds of documented supernova remnants within the Milky Way galaxy (Green 2019; Ranasinghe & Leahy 2022). Many supernova remnants are detected in the radio band, but since we're interested in hard X-rays and gamma rays, the number of potentially observable remnants substantially exceeds the size of the currently detected population due to emission from decaying long-lived radioisotopes. Additionally, more remnants may remain undetected due to close proximity to the galactic center. As such, we use this section to construct a model supernova remnant distribution.

While the kicks and delay times associated with compact binary mergers likely erase any azimuthal structure that may have existed in their progenitor system distribution, core-collapse supernovae are less mobile and occur on much shorter timescales. Supernovae in spiral galaxies are concentrated in or near the spiral arms, with a decaying exponential radial distribution from the galactic center (Petrosian et al. 2005; Maza & van den Bergh 1976; Bartunov et al. 1994; Hakobyan et al. 2009; Barbon et al. 1975). Following the fits outlined in Reid et al. (2014), we construct a five-arm log-spiral model,

where for each arm,

$$R_{\rm spine}(\beta; R_{\rm ref}, \beta_{\rm ref}, \psi) = R_{\rm ref}e^{-(\beta-\beta_{\rm ref})\tan\psi}. \qquad (23)$$

Here, $R_{\rm spine}$ is the galactocentric radius at azimuth β, $R_{\rm ref}$ is a reference radius at azimuth $\beta_{\rm ref}$, and ψ is the pitch angle of the spiral. Motivated by the shapes of the distributions of supernova locations relative to spiral arms in Maza & van den Bergh (1976) and Bartunov et al. (1994), we model the surface density of the ith arm $\sigma_{\rm arm, i}$ as

$$\sigma_{\rm arm, i} \propto \exp\{-\left[R - R_{\rm spine}(\beta; \beta_{\rm ref, i}, \psi_i)\right]^2/w_{\rm arm, i}^2\}, \qquad (24)$$

where $w_{\rm arm}$ is the arm width (a parameter reported in Reid et al. (2014)). For the radial distribution of supernovae, we assume a decaying exponential with scale length $R_s = R_{\rm SN}/R_{25} \sim 0.29$ (Hakobyan et al. 2009), where $R_{25} \sim 13.4\,{\rm kpc}$ for the Milky Way (Goodwin et al. 1998). We also introduce a central depletion factor $f(r) = (R/R_s)^2$ for $R < R_s$ to account for the lack of observed supernovae near the centers of spiral galaxies, which may not be solely due to observational limitations. The total surface density $\sigma_{\rm SN}$ of supernovae in the galaxy is then

$$\sigma_{\rm SN}(R, \beta) \propto e^{-R/R_s}f(R < R_s)\sum_{i=1}^{5}\sigma_{\rm arm, i}. \qquad (25)$$

This surface density is plotted in log-color scale in Fig. 8, with the solar orbital radius shown for scale.

To account for the vertical thickness of the distribution, we include an additional exponential factor for the z coordinate, adopting a vertical scale height $z_s = 100\,{\rm pc}$ motivated by the distribution of vertical positions of supernovae from the catalog presented in Ferrand & Safi-Harb (2012). The full volume density $\rho_{\rm SN}$ is then

$$\rho_{\rm SN}(R, \beta, z) \propto e^{-z/z_s}e^{-R/R_s}f(R < R_s)\sum_{i=1}^{5}\sigma_{\rm arm, i}. \qquad (26)$$

The radial distribution of these positions are plotted against the high-energy supernova remnant catalog from Ferrand & Safi-Harb (2012) in Fig. 9.

4. REMNANT PROPERTIES

4.1. Ejecta Mass

Ejecta masses from neutron star-neutron star mergers are generally thought to be between $\sim 10^{-4} - 10^{-2}\,{\rm M_\odot}$ (Shibata & Hotokezaka 2019; Bauswein et al. 2013; Hotokezaka et al. 2013; Radice et al. 2018). Since the StarTrack model data did not directly report these, but did include the masses of the compact objects for each
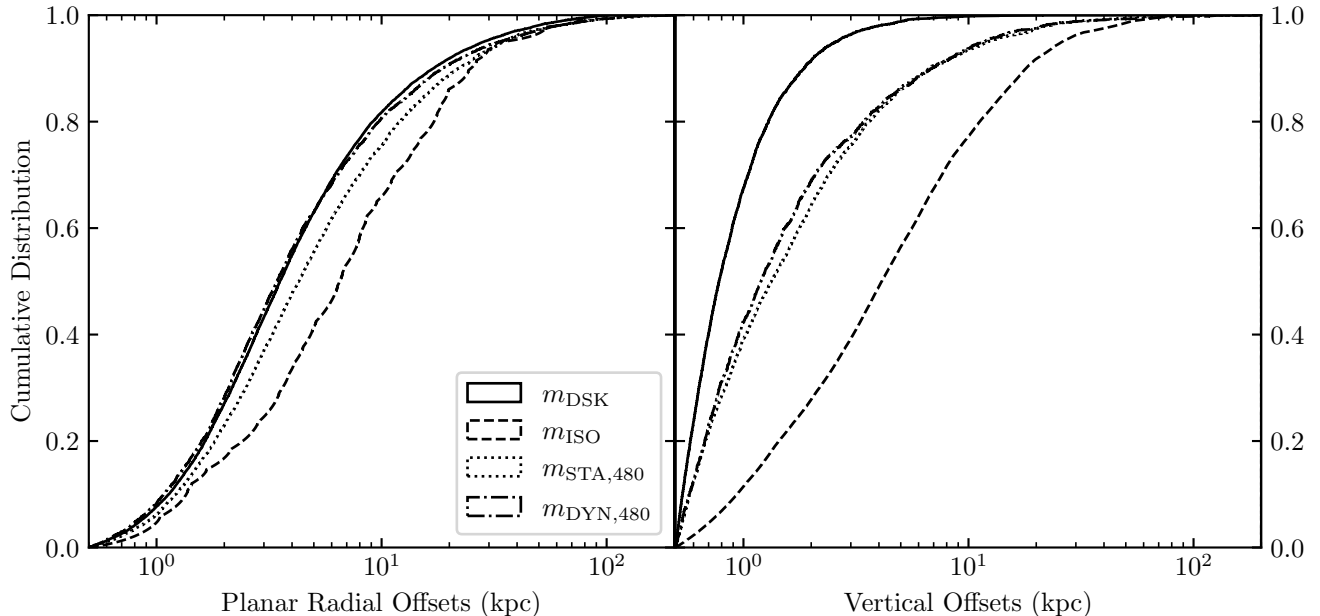
Figure 7. The cumulative distribution functions for compact binary merger planar radial offsets (R) and vertical offsets (z) for the disk (m_{DSK}), isotropic (m_{ISO}), static orbital (m_{STA}), and dynamic orbital (m_{DYN}) models. The offset distributions are practically identical for the population synthesis models M.380B and M.480B, so only the results from M.480B are included here for clarity.
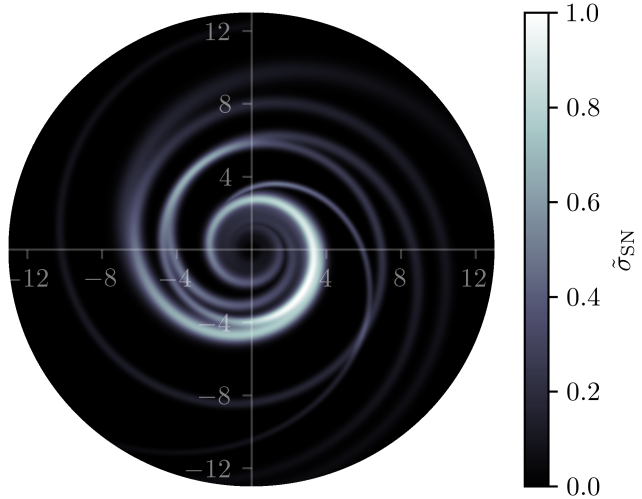

Figure 8. Model surface density of core-collapse supernova locations in the Milky Way (Eq. 25). Indicated distances are in units of kpc.

Figure 9. Cumulative distributions of supernova remnant locations relative to the galactic center. The solid curve is our model distribution, and the dashed curve is the distribution from the catalog in Ferrand & Safi-Harb (2012).

merger, we used an empirical fitting formula presented in Dietrich & Ujevic (2017) to estimate ejecta masses. The distribution of ejecta masses assuming solar metallicity is shown in Fig. 10 for `StarTrack` models M380 and M480.

Supernovae generally eject much larger quantities of material, but only a small fraction of this ejecta is thought to be comprised of r-process elements. Typical estimates tend to be $\sim 10^{-6} - 10^{-4}\,\mathrm{M}_\odot$ (Hoffman et al.

1997; Fryer et al. 2006; Metzger et al. 2007; Mösta et al. 2018), so for the purposes of this project, we uniformly sample masses from this range.

4.2. *Remnant Size*

Both kilonovae and supernovae can be modeled as spherical explosions in a tenuous ambient medium that
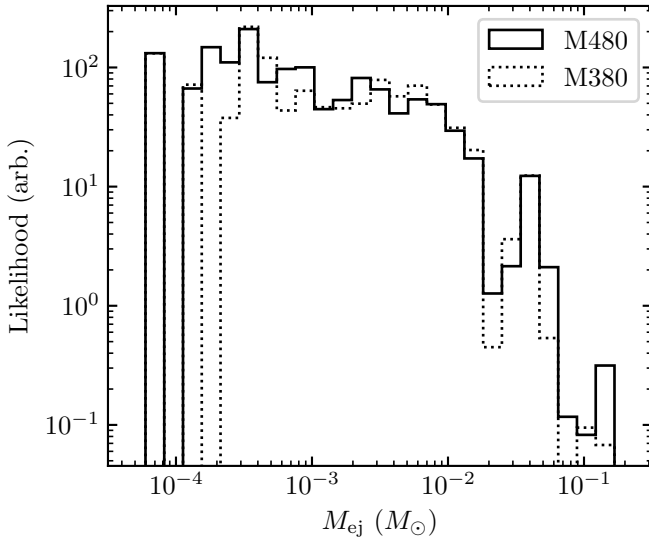
Figure 10. Distribution of neutron star-neutron star merger ejecta masses for progenitors with solar metallicity. These masses were calculated from the empirical formula presented in Dietrich & Ujevic (2017), using neutron star masses taken from `StarTrack` models M380 and M480.

start out mildly relativistic and freely expanding, but ultimately relax into Sedov-Taylor-like blast waves (Taylor 1950). As the ejecta thrown off from the merger at $v_{\rm ej} \sim 0.1c$ pushes outward into the ISM, forward and reverse shocks propagate from the contact discontinuity. While the position of the forward shock is well modeled by self-similar solutions in the Sedov-Taylor phase, this is distinct from the position of the contact discontinuity, which traces the outer boundary of the ejecta cloud. This ejecta is decelerated over a length comparable to the Sedov-Taylor length scale, where the swept up mass equals the ejecta mass.

The emission lines of interest from kilonova remnants come from the r-process material in the ejecta itself, so when we discuss the sizes of kilonova remnants, we are referring to the extent of the ejecta, not the forward shock. Terminal remnant sizes can then be estimated to be approximately equivalent to the deceleration lengths - quantities that only depend on the ejecta mass and the ambient medium density (e.g. Amend et al. 2022). Ambient medium number densities in our model range from $\sim 10^{-4} - 10^{2}\,\mathrm{cm^{-3}}$, consistent with the environments suggested in Wiggins et al. (2018), and resulting in typical kilonova remnant sizes on the order of a few parsecs to tens of parsecs (Fig. 11). These absolute sizes correspond to apparent sizes of $\lesssim 5°$ - often much, much smaller ($\sim$ tens of arcseconds) - for distances $\gtrsim 100\,\mathrm{pc}$.

r-Process from supernovae is expected to be produced either in the wind of the neutron star formed in the explosion or fallback accretion on this neutron star (Hoff-
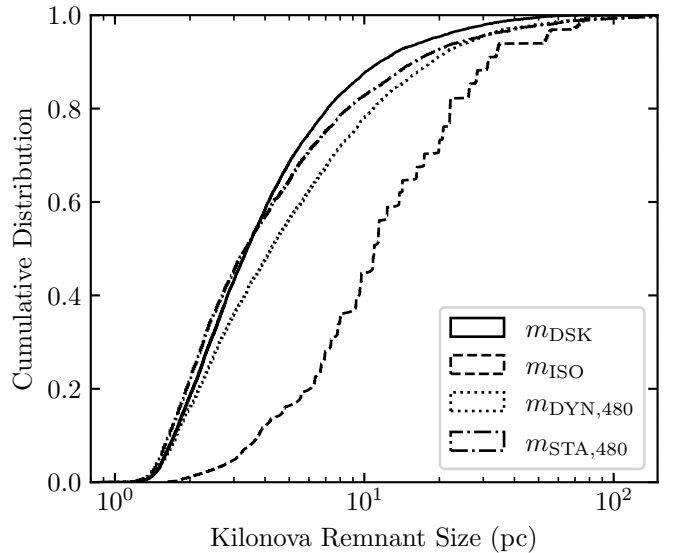
Figure 11. Distribution of kilonova remnant sizes for the disk ($m_{\rm DSK}$), isotropic ($m_{\rm ISO}$), static orbital ($m_{\rm STA,480}$), and dynamic orbital ($m_{\rm DYN,480}$) models. The remnant sizes are practically identical for the population synthesis models M.380B and M.480B, so as was the case for the radial offsets, only the results from M.480B are included here for clarity. Remnant sizes are comparable for the disk and both orbital models at $\sim$ a few pc, while the remnants are larger in the isotropic model ($\sim$ a few tens of pc) due to the low-density environments of the more broadly distributed merger sites.

man et al. 1997; Fryer et al. 2006; Metzger et al. 2007; Mösta et al. 2018). As such, the r-process ejecta will be in the innermost portion of the supernova ejecta, even more centrally concentrated than the ^{44}Ti ejecta. Studies of the ^{44}Ti distribution in supernova remnants (e.g Grefenstette et al. 2014) to place upper limits on this mixing. This extent of the r-process will be a fraction of the extent of the total remnant. The size of the remnant increases with ejecta mass but decreases with the mass of surrounding material. Supernova remnants have more mass than kilonova remnants (leading to larger remnants) but they expand into denser stellar-wind media. There are also extensive catalogs of young galactic supernova remnants that are $\sim$ a few degrees in the sky (Green 2019) and we use these to guide our assumptions about the sizes of the supernova remnants in this work.

5. R-PROCESS GAMMA RAY SPECTRA

To estimate the γ-ray signal coming from the r-process, we combine simulations of nucleosynthesis with evaluated nuclear data. Prompt nucleosynthesis of the r-process as well as the subsequent transmutations of nuclear species on much longer timescales is tracked in the Portable Routines for Integrated nucleoSynthesis Modeling (PRISM) reaction network (Sprouse et al.

2021). The theoretical nuclear inputs (Kawano et al. 2016; Mumpower et al. 2016; Mumpower et al. 2020, 2022) for the network calculation are based on the 2012 version of the Finite-Range Droplet Model (Möller et al. 2015, 2016). This information is supplemented with measured and evaluated data when applicable (Wang et al. 2021; Kondev et al. 2021). The trajectory that defines r-process conditions is taken from Rosswog et al. (2013) with nuclear self-heating. This trajectory produces a main r-process and is subjected to robust fission deposition. We note that most of the relatively short-lived species undergoing fission do not significantly impact γ-ray signals on the remnant timescale; hence we do not include the contribution of fission γ-rays here. For a detailed analysis of γ-rays from fission processes, consult Wang et al. (2020).

The radioactive decay spectra associated with long-lived isotopes (relative to the timescale of the r process) are well known and contained in the eighth version of the Evaluated Nuclear Reaction Data Library (ENDF/B-VIII.0) (Brown et al. 2018). Photons emerging from direct transitions in the nucleus and subsequent scattering processes, including X-ray emission from the de-excitation of atomic states and Augur electrons, are provided by this database.

The abundance information from PRISM is combined with γ-ray emission data from ENDF to produce time-dependent spectra,

$$S(E,t) = N_A \sum_i \lambda_i Y_i(t) \sum_j I_j^\gamma E_j^\gamma \delta(E - E_j^\gamma) \quad (27)$$

where N_A is Avogadro's number, the index i represents the nuclear species with decay rate λ_i and abundance, Y_i, and the index j represents an associated γ-ray with intensity I_j and energy E_j^γ, as in Korobkin et al. (2020).

Equation 27 convolves the population of nuclear species, with the decay rate, with the intensity of γ-ray emission. In order to have significant influence on the spectrum, a nuclear species generally needs a balance of these quantities at a given observational time. We plot in Fig. 12 an example of our synthetic spectra at $t = 100\,\mathrm{kyr}$ and $t = 1\,\mathrm{Myr}$ to showcase this point. The $\sim$ MeV region is dominated by lines from ^{126}Sb, while the $\sim \mathrm{keV} - 100\,\mathrm{keV}$ region consists of a series of prominent lines from ^{126}Sn and ^{229}Th. There has been some recent interest in the 2.6 MeV gamma-ray line from the decay of ^{208}Tl - while this line is not included in our synthetic spectra due to its extremely short half-life ($\sim$3 minutes), it is an interesting case to consider. This nucleus resides at the end of several actinide decay chains, such as that of ^{232}Th, which has a half-life $\sim$ Gyr, meaning it could in principle trace r-process nucleosynthesis

sites. However, given the observational timescales discussed in this paper, the detectability of this line remains highly uncertain, and is left for future work.

6. DETECTABILITY PROSPECTS

To detect these spectra, candidate instruments must have narrow line sensitivities in the right energy range ($\sim 10\,\mathrm{keV} - \mathrm{MeV}$), have sufficiently fine spectral resolution (ideally no more than $\sim$ a few %, though we can still glean information even if some of the lines are blended together), and should be able to effectively separate observations from the gamma ray background (i.e. angular resolution $\lesssim$ a few degrees). Additionally, detectability prospects should generally improve with enhanced sensitivity and larger field of view. Based on these criteria, we have selected COSI as our primary instrument of study. COSI is ideal for this project due to its narrow-line sensitivities, wide field of view, and high spectral resolution. For hard X-Rays, we initially considered HEX-P in spite of its narrow field of view due to its extremely high sensitivity at $\sim$ tens of eV - as HEX-P was not selected and funded, however, we consider a hypothetical instrument with similar specifications.

To predict the number of remnants potentially detectable by COSI and a HEX-P-like instrument, we randomly sample event locations from the distributions generated by our suite of models. These events are sampled within a temporal window of 1 Myr, and the number and timing of events are determined by the event rate $\mathcal{R}$. We assign synthetic spectra to each event based on the elapsed time between the event itself and the present-day, and we calculate the associated photon fluxes based on the ejecta masses and distances. Finally, we compare these predicted fluxes to the narrow-line sensitivities of the relevant instruments to determine whether an event is 'detected'.

Previous exploratory studies on this subject also accounted for the effects that remnant size and doppler broadening might have on possible detections - i.e. if a remnant is too large in the sky, it may be unresolvable as a point source, and if the ejecta is moving too quickly, doppler broadening may significantly lower the flux for any given narrow line. We do not explicitly include these factors in our analysis as we expect the ejecta to be compact and slow-moving at late times, and attribute the aforementioned concerns to erroneously modeling the remnant size using prescriptions for the forward shock rather than the contact discontinuity that marks the outer boundary of the ejected material. Furthermore, because the timescales associated with this deceleration are $\ell_\mathrm{dec}/v_\mathrm{ej} < 10^4$ yr, we assume the effects of doppler
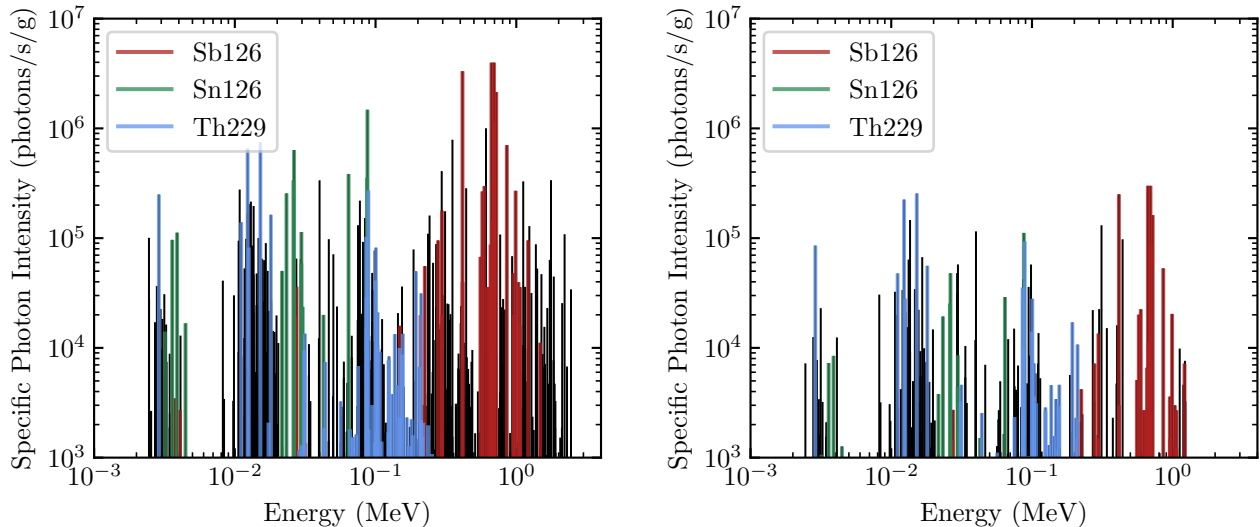
Figure 12. Snapshots of our time-evolving r-process spectra at $t = 100\,\mathrm{kyr}$ (left) and $t = 1\,\mathrm{Myr}$ (right), with some of the most prominent contributing nuclei indicated.

broadening on the spectra are negligible as we are only concerned with gamma ray emission at $\sim 10^4 - 10^6$ yr.

Additional consideration should be given to the remnant sizes, however. While kilonova remnants are expected to be small enough to be localizable as point sources, supernova remnants are much more extended, potentially posing problems for detection against the gamma ray and hard X-ray backgrounds. Catalogs of known galactic supernova remnants include members with sizes on the order of several degrees in the sky, which could be particularly problematic for HEX-P given its sharp angular resolution. Because this issue is more prevalent in supernova remnant detections, it is worth noting that while our results could be informative for these remnants, running high-resolution surveys of known SNRs is likely the best strategy for searching for r-process gamma ray/hard X-ray signatures in this context.

We present our results for COSI and a HEX-P-like instrument respectively in the following subsections, and conclude this section with predictions from a hypothetical future COSI-like instrument with enhanced sensitivity to explore how these detection prospects could change in the coming decades.

6.1. COSI

The COmpton Spectrometer and Imager (COSI) is a Compton telescope that will use novel germanium detectors to provide high-resolution spectroscopy and imaging of gamma rays (Tomsick et al. 2019, 2023). COSI boasts not only high spectral and angular resolution ($\sim 0.8 - 1.1\%$ and 2.1°-4.5° FWHM, respectively), but

all-sky coverage in a day and narrow line sensitivities $\sim 3.0 \times 10^{-6} - 1.2 \times 10^{-5}$ photons $\cdot$ cm$^{-2} \cdot$ s^{-1} - roughly an order of magnitude more sensitive than INTEGRAL SPI in the vicinity of 1 MeV. COSI's high sensitivity taken together with its crisp spectral and angular resolutions make it an ideal candidate for detection of the gamma ray emission lines from decaying r-process material. Additionally, its wide field of view is crucial for this project since the predicted regions of the sky in which these kilonova remnants are expected to exist are not well localized.

We present predictions for the number N of detectable remnants assuming a kilonova event rate $\mathcal{R}_{\mathrm{KN}} = 10^{-5}\,\mathrm{yr}^{-1}$ in Tab. 1, on the rarer side of estimates from LIGO/Virgo (Abbott et al. 2023) for a Milky-Way-like galaxy (when combined with the local galaxy number density). Given this, the most optimistic predictions suggest detection likelihoods $\sim$ a few %, with lower rates dropping this to a fraction of a percent. Similarly, assuming a supernova rate $\mathcal{R}_{\mathrm{SN}} = 10^{-2}\,\mathrm{yr}^{-1}$ (e.g. Rozwadowska et al. (2021)), detection likelihoods are $\sim 1\%$, assuming the remnants are compact enough to even be resolved by the instruments in the first place (Sec. 4.2).

It could be instructive to consider a hypothetical COSI-like instrument (e.g. comparable energy band, angular resolution, and sky coverage) with enhanced sensitivity to explore detection prospects for potential future missions. To raise detection likelihoods to $\sim$ tens of % across all models assuming the same aforementioned

Table 1. Number of kilonova and supernova remnants detectable by COSI over a 24-month survey with 3σ limits assuming event rates of $\mathcal{R}_{\mathrm{KN}} = 10^{-5}\,\mathrm{yr}^{-1}$ and $\mathcal{R}_{\mathrm{SN}} = 10^{-2}\,\mathrm{yr}^{-1}$.

Model	N
Kilonova Remnants	
Disk	4.219×10^{-3}
Static Orbital M380	2.019×10^{-3}
Static Orbital M480	2.189×10^{-3}
Dynamic Orbital M380	1.639×10^{-3}
Dynamic Orbital M480	2.015×10^{-3}
Isotropic	1.261×10^{-3}
Supernova Remnants	
Model Distribution	3.439×10^{-3}
FSH 2012	3.061×10^{-3}

Table 2. Number of kilonova and supernova remnants detectable by a COSI-like instrument with $20\times$ greater sensitivity over a 24-month survey with 3σ limits assuming event rates of $\mathcal{R}_{\mathrm{KN}} = 10^{-5}\,\mathrm{yr}^{-1}$ and $\mathcal{R}_{\mathrm{SN}} = 10^{-2}\,\mathrm{yr}^{-1}$.

Model	N
Kilonova Remnants	
Disk	1.282×10^{-1}
Static Orbital M380	1.918×10^{-1}
Static Orbital M480	1.624×10^{-1}
Dynamic Orbital M380	1.118×10^{-1}
Dynamic Orbital M480	1.517×10^{-1}
Isotropic	6.338×10^{-2}
Supernova Remnants	
Model Distribution	1.867×10^{-2}
FSH 2012	1.699×10^{-2}

event rates, the observing instrument must be ~ 20 times more sensitive. We present detectability prospect predictions for a $20\times$ sensitivity enhancement in Tab. 2, though we note that a lower sensitivity enhancement combined with a longer observing cycle could produce similar results.

For a more detailed exploration of the detectability prospects for similar COSI-like instruments, Fig. 13 shows the fraction of detected kilonova remnants as a
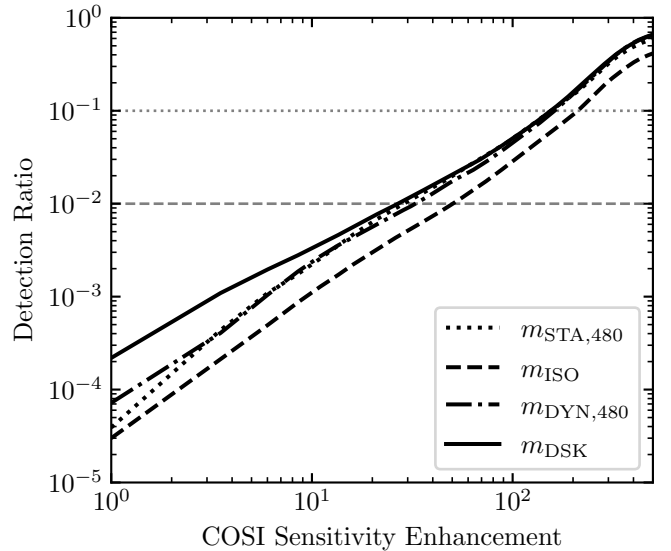
Figure 13. Fraction of detected kilonova remnants vs. COSI sensitivity enhancement. The shaded region corresponds to the fractions spanned by all of our different models, and the horizontal lines represent detection thresholds for each event rate. Note that if the events are extremely rare (e.g. $\mathcal{R} = 10^{-6}\,\mathrm{yr}^{-1}$), detection is nearly impossible even for sensitivity enhancements of several hundred times.

function of sensitivity enhancement. Note that for a detection to be likely, an enhancement on the order of a few factors of ten is needed.

6.2. HEX-P-like Instrument

For a more targeted search, the High Energy X-ray Probe (HEX-P) would have been extremely sensitive to hard X-rays from these kilonova remnants in the $0.2 - 80\,\mathrm{keV}$ range (Madsen et al. 2024). With a spectral resolution of $\sim 2\%$ FWHM at $20\,\mathrm{keV}$, HEX-P would have been able to resolve these hard X-ray lines in principle, especially for older remnants where doppler broadening effects are not as pronounced. HEX-P's sensitivity would have greatly outmatched that of COSI by several orders of magnitude (see Fig. 16), with the tradeoff being an extremely small field of view: $11.3'' \times 11.3''$ for the Low-Energy Telescope (LET), and $13.7'' \times 13.7''$ for the High-Energy Telescope (HET). As such, a HEX-P-like instrument would only be an effective search tool for surveys over extremely small regions of the sky, or for targeting specific remnant candidates.

Given that the sensitivity of such an instrument would be orders of magnitude improved over COSI - though in a slightly lower energy range - if the instrument is pointed in the right direction, it is essentially guaranteed that the sensitivity will be sufficient for a detection as long as the distance to the source is $\lesssim 50\,\mathrm{kpc}$. Candidates for KNRs have been proposed (e.g. Liu et al.

Table 3. Number of kilonova remnants detectable in a HEX-P-like survey in a small region surrounding the galactic center assuming an event rate of $\mathcal{R}_{\mathrm{KN}} = 10^{-5}\,\mathrm{yr}^{-1}$.

Model	N
$0.5^{\circ} \times 0.5^{\circ}$	
Disk	4.900×10^{-2}
Static Orbital M380	5.000×10^{-2}
Static Orbital M480	3.800×10^{-2}
Dynamic Orbital M380	6.800×10^{-2}
Dynamic Orbital M480	8.200×10^{-2}
Isotropic	3.270×10^{-3}
$2^{\circ} \times 2^{\circ}$	
Disk	5.643×10^{-1}
Static Orbital M380	5.040×10^{-1}
Static Orbital M480	4.920×10^{-1}
Dynamic Orbital M380	6.780×10^{-1}
Dynamic Orbital M480	5.820×10^{-1}
Isotropic	5.466×10^{-2}
$5^{\circ} \times 5^{\circ}$	
Disk	1.945×10^{0}
Static Orbital M380	1.684×10^{0}
Static Orbital M480	1.658×10^{0}
Dynamic Orbital M380	2.050×10^{0}
Dynamic Orbital M480	2.016×10^{0}
Isotropic	3.716×10^{-1}

2019), but perhaps beyond this, a more lucrative approach may be to survey known SNRs that may have been misclassified. Details on this strategy, as well as a list of some of the closest such remnants, can be found in Wu et al. (2019). However, due to the larger sizes of supernova remnants, they would likely be difficult to separate from the galactic background using an instrument with such fine angular resolution. As such, for the purposes of this work we consider the KNR detectability prospects for a handful of small surveys surrounding the galactic center, of sizes $0.5^{\circ} \times 0.5^{\circ}$, $2^{\circ} \times 2^{\circ}$, and $5^{\circ} \times 5^{\circ}$. The detection likelihoods for these mock surveys are presented in Tab. 3.

Due to the concentration of events near the galactic midplane, kilonova remnant detections are most likely for low-latitude surveys - the sensitivity of a HEX-P-like instrument offers huge improvements over that of a COSI-like instrument, as can be seen by comparing Fig. 14 to Fig. 15.
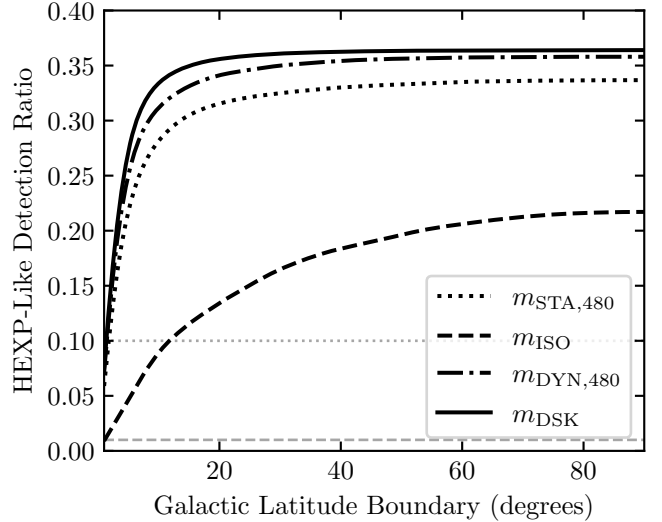
Figure 14. Fraction of detected kilonova remnants bound within varying galactic latitudes for a HEXP-like instrument (e.g. sharing the same sensitivity curve, but only looking out to a maximum distance of $8.1\,\mathrm{kpc}$). The gray dashed and dotted lines represent $\mathcal{R} = 10^{-4}\,\mathrm{yr}^{-1}$ and $\mathcal{R} = 10^{-5}\,\mathrm{yr}^{-1}$, respectively.
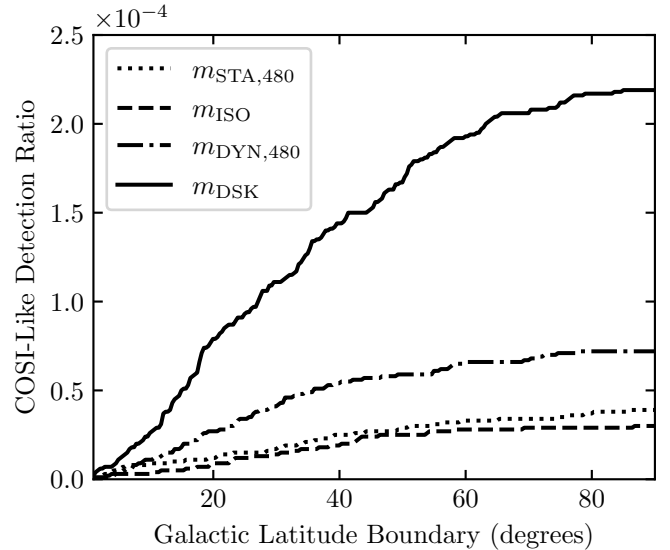
Figure 15. Fraction of detected kilonova remnants bound within varying galactic latitudes for a COSI-like instrument (e.g. sharing the same sensitivity curve). Note that the detection fractions are much smaller for this instrument than they would be for a HEX-P-like mission.

7. SUMMARY

In this work, we explored the detectability prospects for long-lived gamma-ray emission from r-process nucleosynthesis in kilonova and supernova remnants. By modeling the distribution of galactic compact binary merger remnants and supernova remnants, we generated
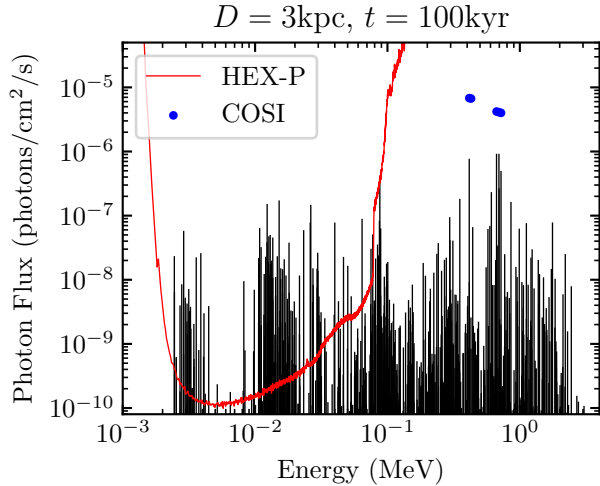
Figure 16. Synthetic spectra for $0.01\,\mathrm{M_\odot}$ of ejecta from a kilonova $3\,\mathrm{kpc}$ away $100\,\mathrm{kyr}$ after the merger, plotted alongside narrow-line sensitivities for COSI and HEX-P.

synthetic spectra of r-process gamma-ray lines and compared them to the sensitivity curves of the future instruments COSI and HEX-P-like missions. Our study shows that while the probability of detecting remnants using current-generation wide-field instruments like COSI is very low, targeted observations with high-sensitivity instruments like HEX-P offer much more promising prospects for detecting galactic r-process events, assuming a suitable target is identified or a small regional survey is feasible. However, identification of such a target and securing the time to run such a large survey using an instrument with a small field of view could be challenging.

Our findings build upon prior studies of r-process gamma-ray diagnostics by addressing key limitations in earlier approaches and refining predictions for observational prospects. Wu et al. (2019) highlighted the importance of emission lines from ^{126}Sn and similar isotopes for identifying neutron star merger remnants in the Milky Way, emphasizing the need for systematic surveys of the Galactic plane. While their approach provided a strong theoretical framework, our work incorporates full synthetic spectra from nuclear reaction networks, and explores different possible distributions for r-process sites in the Milky Way. Similarly, Korobkin et al. (2020) explored gamma-ray emission during both the kilonova phase and later epochs, using radiative transport simulations to show how isotopic fingerprints could constrain ejecta properties; however, spatial distributions of kilonova remnants were not explored as detection probabilities were not an explicit focus of this work. Additionally, as COSI narrow-line sensitivity data

was not yet available, continuum sensitivities were used instead - a limitation that resulted in overly-optimistic predictions that do not carry over to our study here. Building on the work done in Wu et al. (2019), Terada et al. (2022) proposed gamma-ray diagnostics based on specific line ratios sensitive to the electron fraction (Y_e) of the ejecta. While we share their emphasis on late-time remnants, our results further incorporate astrophysical uncertainties, such as ejecta mass, energetics, and remnant site distributions. By integrating these advancements, our study corroborates the broader feasibility of detecting r-process gamma-ray lines while also contributing to the roadmap for future observational strategies.

Ultimately, no single instrument currently combines all the necessary properties to maximize the chances of detection. An ideal instrument would balance the wide field of view characteristic of all-sky survey instruments like COSI with the enhanced sensitivity and fine resolution of targeted instruments similar to HEX-P. To enhance detection prospects, a hypothetical instrument should possess several key properties. First, a wide field of view is crucial, as the locations of potential remnants within the Milky Way are not well constrained. COSI's ability to provide all-sky coverage within a day is a significant advantage, enabling efficient surveys of large sky areas. However, an instrument capable of surveying broad regions while achieving higher sensitivity would be preferable, as COSI's current sensitivity is insufficient to make detections probable. Our results suggest that an instrument with at least ten times COSI's sensitivity would be necessary to raise detection probabilities above $\sim$ a few %, and achieving such sensitivity over a wide field of view could be technically challenging due to constraints in detector technology and instrument design.

In addition to a wide FOV, high sensitivity across the relevant energy ranges is essential. The sensitivity of a HEX-P-like instrument in the hard X-ray band would far exceed that of COSI, rendering it well-suited for targeted observations. However, the narrow field of view would limit its utility for wide surveys. A future instrument that combines HEX-P-like sensitivity with the broad coverage of COSI would significantly improve detection prospects for kilonova remnants. Such an instrument would also require fine spectral and angular resolution: detecting faint gamma-ray lines necessitates a spectral resolution of a few percent to effectively distinguish r-process signatures from background radiation, and an angular resolution of a few degrees is necessary to resolve remnants and differentiate them from diffuse galactic emission. Balancing high sensitivity, fine reso-

lution, and a wide field of view represents a substantial technical challenge due to inherent trade-offs in instrument design and detector capabilities. Balancing these properties would be a primary challenge in designing an optimal mission, as enhancing sensitivity often comes at the expense of field of view due to limitations in detector area and readout capabilities. Future gamma-ray telescopes will need to carefully navigate this trade-off to maximize the chances that faint, widely distributed sources like kilonova remnants can be effectively detected.

REFERENCES

Abbott, R., Abbott, T. D., Acernese, F., et al. 2023, Physical Review X, 13, 011048, doi: 10.1103/PhysRevX.13.011048

Amend, B., Zrake, J., & Hartmann, D. H. 2022, ApJ, 939, 59, doi: 10.3847/1538-4357/ac951b

Argast, D., Samland, M., Thielemann, F. K., & Qian, Y. Z. 2004, A&A, 416, 997, doi: 10.1051/0004-6361:20034265

Barbon, R., Capaccioli, M., & Ciatti, F. 1975, A&A, 44, 267

Barnes, J., Zhu, Y. L., Lund, K. A., et al. 2021, ApJ, 918, 44, doi: 10.3847/1538-4357/ac0aec

Bartunov, O. S., Tsvetkov, D. Y., & Filimonova, I. V. 1994, PASP, 106, 1276, doi: 10.1086/133505

Bauswein, A., Goriely, S., & Janka, H. T. 2013, ApJ, 773, 78, doi: 10.1088/0004-637X/773/1/78

Belczynski, K., Kalogera, V., & Bulik, T. 2002, ApJ, 572, 407, doi: 10.1086/340304

Belczynski, K., Kalogera, V., Rasio, F. A., et al. 2008, ApJS, 174, 223, doi: 10.1086/521026

Belczynski, K., Perna, R., Bulik, T., et al. 2006, ApJ, 648, 1110, doi: 10.1086/505169

Belokurov, V., Erkal, D., Evans, N. W., Koposov, S. E., & Deason, A. J. 2018, MNRAS, 478, 611, doi: 10.1093/mnras/sty982

Berger, E., Fong, W., & Chornock, R. 2013, ApJL, 774, L23, doi: 10.1088/2041-8205/774/2/L23

Blanchard, P. K., Berger, E., & Fong, W.-f. 2016, ApJ, 817, 144, doi: 10.3847/0004-637X/817/2/144

Blanchard, P. K., Berger, E., Fong, W., et al. 2017, ApJL, 848, L22, doi: 10.3847/2041-8213/aa9055

Bloom, J. S., Sigurdsson, S., & Pols, O. R. 1999, MNRAS, 305, 763, doi: 10.1046/j.1365-8711.1999.02437.x

Brown, D. A., Chadwick, M. B., Capote, R., et al. 2018, Nuclear Data Sheets, 148, 1 , doi: 10.1016/j.nds.2018.02.001

Burbidge, E. M., Burbidge, G. R., Fowler, W. A., & Hoyle, F. 1957, Reviews of Modern Physics, 29, 547, doi: 10.1103/RevModPhys.29.547

Cameron, A. G. W. 1957, PASP, 69, 201, doi: 10.1086/127051

Conselice, C. J. 2014, ARA&A, 52, 291, doi: 10.1146/annurev-astro-081913-040037

Côté, B., Eichler, M., Arcones, A., et al. 2019, ApJ, 875, 106, doi: 10.3847/1538-4357/ab10db

Cowan, J. J., Sneden, C., Lawler, J. E., et al. 2021, Reviews of Modern Physics, 93, 015002, doi: 10.1103/RevModPhys.93.015002

Dietrich, T., & Ujevic, M. 2017, Classical and Quantum Gravity, 34, 105014, doi: 10.1088/1361-6382/aa6bb0

Eichler, D., Livio, M., Piran, T., & Schramm, D. N. 1989, Nature, 340, 126, doi: 10.1038/340126a0

Feltzing, S., Holmberg, J., & Hurley, J. R. 2001, A&A, 377, 911, doi: 10.1051/0004-6361:20011119

Ferrand, G., & Safi-Harb, S. 2012, Advances in Space Research, 49, 1313, doi: 10.1016/j.asr.2012.02.004

Flynn, C., Holmberg, J., Portinari, L., Fuchs, B., & Jahreiß, H. 2006, MNRAS, 372, 1149, doi: 10.1111/j.1365-2966.2006.10911.x

Fong, W.-f., Nugent, A. E., Dong, Y., et al. 2022, ApJ, 940, 56, doi: 10.3847/1538-4357/ac91d0

Frankel, N., Sanders, J., Rix, H.-W., Ting, Y.-S., & Ness, M. 2019, ApJ, 884, 99, doi: 10.3847/1538-4357/ab4254

Freiburghaus, C., Rosswog, S., & Thielemann, F. K. 1999, ApJL, 525, L121, doi: 10.1086/312343

Fryer, C. L., Herwig, F., Hungerford, A., & Timmes, F. X. 2006, ApJL, 646, L131, doi: 10.1086/507071

Fryer, C. L., Woosley, S. E., & Hartmann, D. H. 1999, ApJ, 526, 152, doi: 10.1086/307992

Fryer, C. L., Hungerford, A. L., Wollaeger, R. T., et al. 2024, ApJ, 961, 9, doi: 10.3847/1538-4357/ad1036

Gaspari, N., Levan, A. J., Chrimes, A. A., & Nelemans, G. 2023, The Galactic neutron star population II – Systemic velocities and merger locations of binary neutron stars. https://arxiv.org/abs/2310.14773

Goodwin, S. P., Gribbin, J., & Hendry, M. A. 1998, The Observatory, 118, 201

Goriely, S., Bauswein, A., & Janka, H.-T. 2011, ApJL, 738, L32, doi: 10.1088/2041-8205/738/2/L32

Green, D. A. 2019, Journal of Astrophysics and Astronomy, 40, 36, doi: 10.1007/s12036-019-9601-6

Grefenstette, B. W., Harrison, F. A., Boggs, S. E., et al. 2014, Nature, 506, 339, doi: 10.1038/nature12997

Hakobyan, A. A., Mamon, G. A., Petrosian, A. R., Kunth, D., & Turatto, M. 2009, A&A, 508, 1259, doi: 10.1051/0004-6361/200912795

Helmi, A., Babusiaux, C., Koppelman, H. H., et al. 2018, Nature, 563, 85, doi: 10.1038/s41586-018-0625-x

Helmi, A., White, S. D. M., de Zeeuw, P. T., & Zhao, H. 1999, Nature, 402, 53, doi: 10.1038/46980

Hoffman, R. D., Woosley, S. E., & Qian, Y. Z. 1997, ApJ, 482, 951, doi: 10.1086/304181

Holmberg, J., Nordström, B., & Andersen, J. 2007, A&A, 475, 519, doi: 10.1051/0004-6361:20077221

Hotokezaka, K., Kiuchi, K., Kyutoku, K., et al. 2013, PhRvD, 87, 024001, doi: 10.1103/PhysRevD.87.024001

Hotokezaka, K., Wanajo, S., Tanaka, M., et al. 2016, MNRAS, 459, 35, doi: 10.1093/mnras/stw404

Jin, Z.-P., Li, X., Cano, Z., et al. 2015, ApJL, 811, L22, doi: 10.1088/2041-8205/811/2/L22

Just, O., Bauswein, A., Ardevol Pulpillo, R., Goriely, S., & Janka, H. T. 2015, MNRAS, 448, 541, doi: 10.1093/mnras/stv009

Kasliwal, M. M., Korobkin, O., Lau, R. M., Wollaeger, R., & Fryer, C. L. 2017, ApJL, 843, L34, doi: 10.3847/2041-8213/aa799d

Kawano, T., Capote, R., Hilaire, S., & Chau Huu-Tai, P. 2016, Physical Review C, 94, doi: 10.1103/PhysRevC.94.014612

Kennicutt, Robert C., J. 1989, ApJ, 344, 685, doi: 10.1086/167834

—. 1998, ApJ, 498, 541, doi: 10.1086/305588

Klypin, A. A., Trujillo-Gomez, S., & Primack, J. 2011, ApJ, 740, 102, doi: 10.1088/0004-637X/740/2/102

Kondev, F., Wang, M., Huang, W., Naimi, S., & Audi, G. 2021, Chinese Physics C, 45, 030001, doi: 10.1088/1674-1137/abddae

Korobkin, O., Rosswog, S., Arcones, A., & Winteler, C. 2012, MNRAS, 426, 1940, doi: 10.1111/j.1365-2966.2012.21859.x

Korobkin, O., Hungerford, A. M., Fryer, C. L., et al. 2020, ApJ, 889, 168, doi: 10.3847/1538-4357/ab64d8

Korobkin, O., Wollaeger, R. T., Fryer, C. L., et al. 2021, ApJ, 910, 116, doi: 10.3847/1538-4357/abe1b5

Lattimer, J. M., & Schramm, D. N. 1974, ApJL, 192, L145, doi: 10.1086/181612

Li, L.-X. 2019, ApJ, 872, 19, doi: 10.3847/1538-4357/aaf961

Lian, J., Zasowski, G., Chen, B., et al. 2024, Nature Astronomy, doi: 10.1038/s41550-024-02315-7

Licquia, T. C., & Newman, J. A. 2015, ApJ, 806, 96, doi: 10.1088/0004-637X/806/1/96

Lilly, S. J., Carollo, C. M., Pipino, A., Renzini, A., & Peng, Y. 2013, ApJ, 772, 119, doi: 10.1088/0004-637X/772/2/119

Liu, Y., Zou, Y.-C., Jiang, B., et al. 2019, MNRAS, 490, L21, doi: 10.1093/mnrasl/slz141

Madau, P., & Dickinson, M. 2014, ARA&A, 52, 415, doi: 10.1146/annurev-astro-081811-125615

Madau, P., & Fragos, T. 2017, ApJ, 840, 39, doi: 10.3847/1538-4357/aa6af9

Madsen, K. K., García, J. A., Stern, D., et al. 2024, Frontiers in Astronomy and Space Sciences, 11, 1357834, doi: 10.3389/fspas.2024.1357834

Malhan, K., Ibata, R. A., Sharma, S., et al. 2022, ApJ, 926, 107, doi: 10.3847/1538-4357/ac4d2a

Matteucci, F., Romano, D., Arcones, A., Korobkin, O., & Rosswog, S. 2014, MNRAS, 438, 2177, doi: 10.1093/mnras/stt2350

Maza, J., & van den Bergh, S. 1976, ApJ, 204, 519, doi: 10.1086/154198

McKee, C. F., Parravano, A., & Hollenbach, D. J. 2015, ApJ, 814, 13, doi: 10.1088/0004-637X/814/1/13

Metzger, B. D., Thompson, T. A., & Quataert, E. 2007, ApJ, 659, 561, doi: 10.1086/512059

Miyamoto, M., & Nagai, R. 1975, PASJ, 27, 533

Möller, P., Sierk, A. J., Ichikawa, T., Iwamoto, A., & Mumpower, M. 2015, Physical Review C - Nuclear Physics, 91, 1, doi: 10.1103/PhysRevC.91.024310

Möller, P., Sierk, A. J., Ichikawa, T., & Sagawa, H. 2016, Atomic Data and Nuclear Data Tables, 109-110, 1, doi: 10.1016/j.adt.2015.10.002

Mösta, P., Roberts, L. F., Halevi, G., et al. 2018, ApJ, 864, 171, doi: 10.3847/1538-4357/aad6ec

Mumpower, M. R., Jaffke, P., Verriere, M., & Randrup, J. 2020, PhRvC, 101, 054607, doi: 10.1103/PhysRevC.101.054607

Mumpower, M. R., Kawano, T., & Möller, P. 2016, Physical Review C, 94, 1, doi: 10.1103/PhysRevC.94.064317

Mumpower, M. R., Kawano, T., & Sprouse, T. M. 2022, PhRvC, 106, 065805, doi: 10.1103/PhysRevC.106.065805

Myeong, G. C., Vasiliev, E., Iorio, G., Evans, N. W., &
Belokurov, V. 2019, MNRAS, 488, 1235,
doi: 10.1093/mnras/stz1770

Navarro, J. F., Frenk, C. S., & White, S. D. M. 1996, ApJ,
462, 563, doi: 10.1086/177173

Nelson, E. J., van Dokkum, P. G., Förster Schreiber, N. M.,
et al. 2016, ApJ, 828, 27,
doi: 10.3847/0004-637X/828/1/27

Nishimura, N., Takiwaki, T., & Thielemann, F.-K. 2015,
ApJ, 810, 109, doi: 10.1088/0004-637X/810/2/109

Nordström, B., Mayor, M., Andersen, J., et al. 2004, A&A,
418, 989, doi: 10.1051/0004-6361:20035959

Olejak, A., Belczynski, K., & Ivanova, N. 2021, A&A, 651,
A100, doi: 10.1051/0004-6361/202140520

Petrosian, A., Navasardyan, H., Cappellaro, E., et al. 2005,
AJ, 129, 1369, doi: 10.1086/427712

Pian, E., D'Avanzo, P., Benetti, S., et al. 2017, Nature,
551, 67, doi: 10.1038/nature24298

Planck Collaboration, Aghanim, N., Akrami, Y., et al.
2020, A&A, 641, A6, doi: 10.1051/0004-6361/201833910

Radice, D., Perego, A., Hotokezaka, K., et al. 2018, ApJ,
869, 130, doi: 10.3847/1538-4357/aaf054

Ranasinghe, S., & Leahy, D. 2022, ApJ, 940, 63,
doi: 10.3847/1538-4357/ac940a

Rastinejad, J. C., Gompertz, B. P., Levan, A. J., et al.
2022, Nature, 612, 223, doi: 10.1038/s41586-022-05390-w

Reid, M. J., Menten, K. M., Brunthaler, A., et al. 2014,
ApJ, 783, 130, doi: 10.1088/0004-637X/783/2/130

Rosswog, S., Liebendörfer, M., Thielemann, F. K., et al.
1999, A&A, 341, 499

Rosswog, S., Piran, T., & Nakar, E. 2013, Mon. Not. R.
Astron. Soc., 430, 2585, doi: 10.1093/mnras/sts708

Rozwadowska, K., Vissani, F., & Cappellaro, E. 2021,
NewA, 83, 101498, doi: 10.1016/j.newast.2020.101498

Schatz, H., Becerril Reyes, A. D., Best, A., et al. 2022,
Journal of Physics G Nuclear Physics, 49, 110502,
doi: 10.1088/1361-6471/ac8890

Schmidt, M. 1959, ApJ, 129, 243, doi: 10.1086/146614

Seeger, P. A., Fowler, W. A., & Clayton, D. D. 1965, ApJS,
11, 121, doi: 10.1086/190111

Shibata, M., & Hotokezaka, K. 2019, Annual Review of
Nuclear and Particle Science, 69, 41,
doi: 10.1146/annurev-nucl-101918-023625

Siegel, D. M., Barnes, J., & Metzger, B. D. 2019, Nature,
569, 241, doi: 10.1038/s41586-019-1136-0

Speagle, J. S., Steinhardt, C. L., Capak, P. L., &
Silverman, J. D. 2014, ApJS, 214, 15,
doi: 10.1088/0067-0049/214/2/15

Sprouse, T. M., Mumpower, M. R., & Surman, R. 2021,
PhRvC, 104, 015803, doi: 10.1103/PhysRevC.104.015803

Surman, R., McLaughlin, G. C., Ruffert, M., Janka, H. T.,
& Hix, W. R. 2008, ApJL, 679, L117, doi: 10.1086/589507

Tak, D., Uhm, Z. L., & Gillanders, J. H. 2023, ApJ, 958,
121, doi: 10.3847/1538-4357/ad06b0

Tanvir, N. R., Levan, A. J., Fruchter, A. S., et al. 2013,
Nature, 500, 547, doi: 10.1038/nature12505

Tanvir, N. R., Levan, A. J., González-Fernández, C., et al.
2017, ApJL, 848, L27, doi: 10.3847/2041-8213/aa90b6

Tarumi, Y., Hotokezaka, K., Domoto, N., & Tanaka, M.
2023, arXiv e-prints, arXiv:2302.13061,
doi: 10.48550/arXiv.2302.13061

Taylor, G. 1950, Proceedings of the Royal Society of
London Series A, 201, 159, doi: 10.1098/rspa.1950.0049

Terada, Y., Miwa, Y., Ohsumi, H., et al. 2022, ApJ, 933,
111, doi: 10.3847/1538-4357/ac721f

Tomsick, J., Zoglauer, A., Sleator, C., et al. 2019, in
Bulletin of the American Astronomical Society, Vol. 51,
98, doi: 10.48550/arXiv.1908.04334

Tomsick, J. A., Boggs, S. E., Zoglauer, A., et al. 2023,
arXiv e-prints, arXiv:2308.12362,
doi: 10.48550/arXiv.2308.12362

Voss, R., & Tauris, T. M. 2003, MNRAS, 342, 1169,
doi: 10.1046/j.1365-8711.2003.06616.x

Wanajo, S., Kajino, T., Mathews, G. J., & Otsuki, K. 2001,
ApJ, 554, 578, doi: 10.1086/321339

Wanajo, S., Sekiguchi, Y., Nishimura, N., et al. 2014,
ApJL, 789, L39, doi: 10.1088/2041-8205/789/2/L39

Wang, M., Huang, W., Kondev, F., Audi, G., & Naimi, S.
2021, Chinese Physics C, 45, 030003,
doi: 10.1088/1674-1137/abddaf

Wang, X., N3AS Collaboration, Vassh, N., et al. 2020,
ApJL, 903, L3, doi: 10.3847/2041-8213/abbe18

Watkins, L. L., van der Marel, R. P., Sohn, S. T., & Evans,
N. W. 2019, ApJ, 873, 118,
doi: 10.3847/1538-4357/ab089f

Watson, D., Hansen, C. J., Selsing, J., et al. 2019, Nature,
574, 497, doi: 10.1038/s41586-019-1676-3

Wiggins, B. K., Fryer, C. L., Smidt, J. M., et al. 2018, ApJ,
865, 27, doi: 10.3847/1538-4357/aad2d4

Winteler, C., Käppeli, R., Perego, A., et al. 2012, ApJL,
750, L22, doi: 10.1088/2041-8205/750/1/L22

Woosley, S. E., Wilson, J. R., Mathews, G. J., Hoffman,
R. D., & Meyer, B. S. 1994, ApJ, 433, 229,
doi: 10.1086/174638

Wu, M.-R., Banerjee, P., Metzger, B. D., et al. 2019, ApJ,
880, 23, doi: 10.3847/1538-4357/ab2593

Yong, D., Kobayashi, C., Da Costa, G. S., et al. 2021,
Nature, 595, 223, doi: 10.1038/s41586-021-03611-2

Zevin, M., Kelley, L. Z., Nugent, A., et al. 2020, ApJ, 904,
190, doi: 10.3847/1538-4357/abc266

Zhu, Y. L., Lund, K. A., Barnes, J., et al. 2021, ApJ, 906, 94, doi: 10.3847/1538-4357/abc69e